

## Phase-field simulation of austenite growth behavior: Insights into the austenite memory phenomenon



Pengcheng Song<sup>a,b,\*</sup>, Yanzhou Ji<sup>b,\*</sup>, Lei Chen<sup>b,c</sup>, Wenbo Liu<sup>a</sup>, Chi Zhang<sup>a</sup>, Long-Qing Chen<sup>b</sup>, Zhigang Yang<sup>a</sup>

<sup>a</sup> Key Laboratory for Advanced Materials of Ministry of Education, School of Materials Science and Engineering, Tsinghua University, Beijing 100084, China

<sup>b</sup> Department of Materials Science and Engineering, The Pennsylvania State University, University Park, PA 16802, USA

<sup>c</sup> Department of Mechanical Engineering, Mississippi State University, MS 39762, USA

### ARTICLE INFO

#### Article history:

Received 3 July 2015

Received in revised form 21 January 2016

Accepted 25 January 2016

Available online 13 February 2016

#### Keywords:

Austenite memory

Reverse austenitic transformation

Crystallography

Bain grouping

Phase-field modeling

### ABSTRACT

Austenite memory phenomenon impedes the application of reverse austenitic transformation to refine grains in steels. In this work, a phase-field model is employed to understand the austenite memory mechanism in terms of austenite growth behaviors under different mechanical boundary conditions, using the Fe–23Ni (wt.%) alloy as an example. The effect of defects formed during martensitic transformation on reverse austenitic transformation is considered by introducing a “stored energy” term. Kurdjumov–Sachs (K–S) variants of each phase are divided into three groups based on the crystallography analysis. Results show that different combinations of mechanical boundary conditions during the austenite → martensite → austenite transformation cycle have different effects on the austenite memory phenomenon, which can be attributed to the minimization of strain energy induced by phase transformations, as well as the inhomogeneous distribution of stored energy (energy of defects).

© 2016 Elsevier B.V. All rights reserved.

### 1. Introduction

Owing to their excellent mechanical properties and low cost, martensitic stainless steels have wide applications in industry [1]. The increasing demand for high-quality steels continuously drives investigations on stainless steels with better mechanical properties. There are several methods to enhance the mechanical properties of steels, among which grain refinement is one of the most effective ways to improve both strength and toughness [2,3]. Grain refinement is usually realized by phase transformations and plastic deformations [4,5]. With severe plastic deformation, it is even possible to obtain ultrafine grain structures [6].

However, for some applications, like the steam turbine rotors used in power plants, plastic deformation is unavailable owing to the large component size and complicated shape [7]. In which case, reverse austenitic transformation could be an effective grain refinement technique [8,9]. Reverse austenitic transformations usually follow certain orientation relationships, e.g., the

Kurdjumov–Sachs (K–S) relation [16,41]. In the case of high alloy martensitic stainless steels, austenite nucleates with an identical crystallographic orientation in one grain and grows into a coarse austenite grain that is crystallographically similar to original austenite grain. This is known as “austenite memory” phenomenon which is detrimental to the grain refinement [10–15]. In order to achieve refined grains in high alloy steels during reverse transformations, it is crucial to understand the underlying mechanisms of the “austenite memory” phenomenon.

Numerous efforts have been made to explain the mechanism behind the “austenite memory” phenomenon [10–20]. For example, it was proposed that coherent acicular-shaped reverse austenite particles form at the martensite lath boundaries with the K–S orientation relationship, leading to the reappearance of prior austenite [19,20]. However, since the reverse transformation occurs at high temperature, the experimental techniques (like TEM, EBSD, XRD, etc.) offer limited insight into the mechanism of the transformation, it has to be observed indirectly by analyzing the quenched microstructures. Undoubtedly, the quenching process affects the uncovering of “austenite memory”.

On the other hand, by formulating the thermodynamic functions and transformation kinetic equations of both austenites and martensites at high temperatures, the high-temperature phase transformation and microstructure evolution processes can be predicted using theoretical methods. Among the existing theoretical

\* Corresponding authors at: Key Laboratory for Advanced Materials of Ministry of Education, Department of Materials Science and Engineering, Tsinghua University, Beijing 100084, China (P. Song). Department of Materials Science and Engineering, The Pennsylvania State University, University Park, PA 16802, USA (Y. Ji).

E-mail addresses: [songpc11@mails.tsinghua.edu.cn](mailto:songpc11@mails.tsinghua.edu.cn) (P. Song), [yxj135@psu.edu](mailto:yxj135@psu.edu) (Y. Ji).

studies [21–33], the phase-field approach stands out as a powerful computational method for modeling phase transformation and microstructure evolution at the meso-scale [25–33]. Moreover, it has been widely used to study martensitic transformations [26,28–35]. With the Bain transformation mechanism and group-subgroup symmetry relationship between the cubic austenite and the tetragonal martensite, three order parameters are usually used to express the crystallographically equivalent Bain variants; morphology and kinetics of martensitic transformations, for instance, habit planes of martensites [30], effect of applied stress or strain on martensitic transformations [31], etc., have been systematically studied.

However, there has been much less focus on the reverse transformation [34]. Reverse austenitic transformations can take place diffusively due to the high temperature whereas under certain conditions (fast heating rate, high content of austenite stabilizer alloy element such as Ni and low C content), it would appear in a displacive manner [10,13,14]. Therefore, to understand the reverse transformation mechanism, we first investigated the crystallography of both martensitic and austenitic transformations. We then performed phase-field simulations of  $\gamma \rightarrow \alpha \rightarrow \gamma$  phase transformation cycle to understand the influence of initial states and mechanical boundary conditions of martensite on reverse transformation and to figure out the austenite growth behaviors that are related to the “austenite memory” phenomenon. Especially, the roles of phase-transformation-induced strain energy for both transformations and the energy of defects are carefully studied, owing to their influence on nucleation site and growth behavior of reverse austenitic transformation [53]. The distribution and amount of these energy contributions under different mechanical boundary conditions are also investigated and related to the “austenite memory” phenomenon through their effects on the nucleation and growth behavior of reverse austenite. The phase transformation cycle in Fe–23Ni alloy is taken as an example, in which the reverse austenitic transformation takes place displacively [37].

## 2. Crystallography of $\gamma \rightarrow \alpha \rightarrow \gamma$ transformations

Both of the martensitic and reverse austenitic transformations proceed diffusively under specific heat treatment conditions in Fe–23Ni [37,38]. The austenite, or  $\gamma$  phase, has a face-centered cubic (fcc) structure while the martensite, or  $\alpha$  phase, is considered to be with a body-centered cubic (bcc) structure. The K–S or, less commonly, other orientation relationships show the crystallographic characteristics of coherent transformation [39,40]. The K–S orientation relationship is expressed as  $\{111\}_\gamma // \{110\}_\alpha$  and  $\langle 110 \rangle_\gamma // \langle 111 \rangle_\alpha$ . The crystallographic correspondences for both transformations are shown in Fig. 1. As illustrated in the figure, for the martensitic transformation, each  $\{111\}_\gamma$  plane defines six crystallographically equivalent variants, resulting in 24 distinguishable K–S variants of the martensite. In addition, the transfer of stacking model from ...ABCABC... of fcc to ...ABAB... of bcc is shown in Fig. 2. For the reverse austenitic transformation, four variants with different orientations are possible when the plane is fixed as  $(011)_\alpha$ . Because the martensite phase has six crystallographically equivalent  $\{110\}_\alpha$  planes, there are also 24 variants of the austenite available during reverse austenitic transformation [16]. The transfer of stacking model from ...ABAB... of bcc to ...ABCABC... of fcc is shown in Fig. 3.

For simplicity, the variants for each transformation can be divided into three groups based on the analysis about the deformation tensors of both transformations. These groups are associated with a particular variant of the “Bain strain” that provides the simplest connection between the austenitic and martensitic structures [16,41,42]. Details are provided in Supplementary materials. In an

existing simulation [34] on reverse austenitic transformation, the crystal structure of martensite was considered to be tetragonal; therefore, Bain strain was only applied to martensitic transformation, while the formation of reverse austenite was equivalent to the disappearance of the martensite. In addition, the effects of transformation-induced strain energy and defect energy on reverse transformations were not considered. However, for bcc martensites, due to the more complicated orientation relationship and the significant effects of strain energy and defect energy, the model in [34] could not reflect the crystallographic and microstructural features. Therefore, in the present work, to determine the effect of reverse austenitic transformation induced strain energy, Bain strain is also considered for modeling the reverse austenitic transformation.

Eqs. (S8) and (S13), and those listed in St1 and St2 (see Supplementary materials) show that the deformation matrices for austenite to martensite transformation contain a major part of Bain deformation, accompanied with a small rotation. The Bain deformation for austenite to martensite transformation is characterized by the compressive axis [41], lying along one of the three cubic axes of austenite, and by which we group those K–S variants of martensite into three kinds. Similarly, the Bain deformation of martensite to austenite transformation is characterized by the tensile axis. It lies along one of the three cubic axes of martensite. We label the K–S variants of both martensite and reverse austenite by their deformation axes  $\{xyz\}$ , as shown in Tables 1 and 2. With the strain of each variant calculated in Section 3.2, each group of variants can be represented by the same Bain strain tensor. Thus, we use three order parameters in the phase-field model to represent three groups of variants:  $\{\eta_1, \eta_2, \eta_3\}$  for the martensite variant groups of martensitic transformation;  $\{\phi_1, \phi_2, \phi_3\}$  for the austenite variant groups of reverse austenitic transformation.

## 3. Phase-field model

The  $\gamma \rightarrow \alpha \rightarrow \gamma$  transformation cycle of Fe–23Ni alloy includes quenching and the subsequent reheating process. The microstructure evolution during cycling is governed by the total free energy minimization within the system. The total free energy includes the Gibbs free energy of the two phases, the interfacial energy at phase boundaries and variants boundaries, as well as the elastic strain energy due to the structural change. The sets of order parameters,  $\{\eta_1, \eta_2, \eta_3\}$  and  $\{\phi_1, \phi_2, \phi_3\}$ , represent different variants of  $\alpha$  and  $\gamma$  phases, respectively. For the martensitic transformation,  $\eta_i=0$  represents the austenite phase and  $\eta_i=1$  represents the martensite phase. For the reverse austenitic transformation,  $\phi_i=0$  represents the martensite phase and  $\phi_i=1$  represents the austenite phase. Then the total free energy of the system is given as [27,43,44]:

$$G_{total} = \int \left[ G_V^{local}(\{\eta_i\}, \{\phi_j\}, T) + G_V^{grad}(\{\nabla\eta_i\}, \{\nabla\phi_j\}) + G_V^{el} \right] dV \quad (1)$$

where  $G_V^{local}(\{\eta_i\}, \{\phi_j\}, T)$  is the temperature dependent local free energy density,  $G_V^{grad}(\{\nabla\eta_i\}, \{\nabla\phi_j\})$  is the gradient energy density due to the inhomogeneity of order parameters at boundaries.  $G_V^{el}$  stands for the density of phase-transformation-induced strain energy.

### 3.1. Local free energy

The driving force for the displacive transformation cycle is the bulk energy difference between the parent phase and the new phase. We employ the Landau-type free energy to describe thermodynamics of the transformation, with its coefficients determined by the relevant physical variables of the specific system,

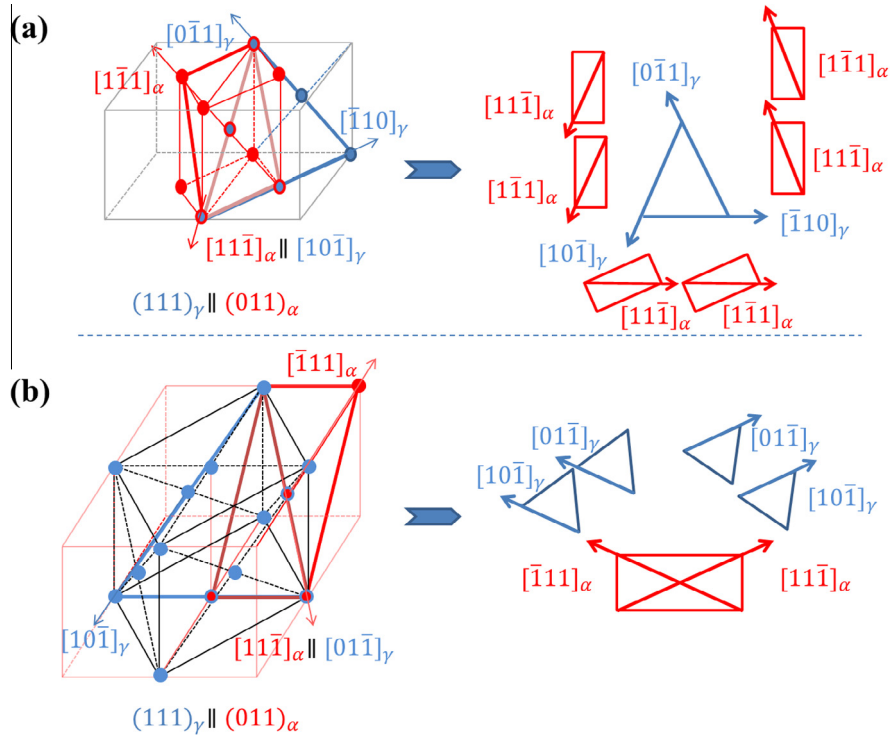


**Fig. 1.** Schematic figures of the atomic correspondence for (a) martensitic transformation, and (b) reverse austenitic transformation. Red dots represent the atoms of martensite, and blue dots represent the atoms of austenite. (For interpretation of the references to color in this figure legend, the reader is referred to the web version of this article.)

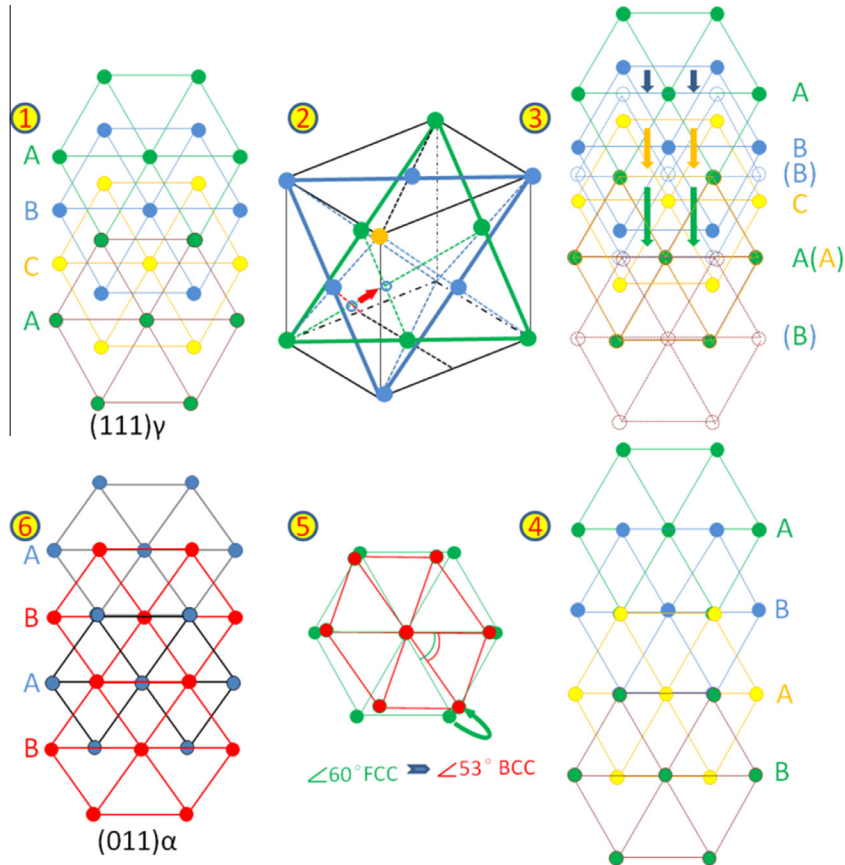


**Fig. 2.** Atomic correspondences for variants of martensite phase with K-S orientation relationship with austenite phase. From ① to ⑥ shows how the face-centered-cubic atom stacking of austenite transform to the body-centered-cubic atom stacking of martensite. Arrows in ②, ③, and ⑤ represent the atomic movement. The dots of the same color mean the same atom plane. (For interpretation of the references to color in this figure legend, the reader is referred to the web version of this article.)

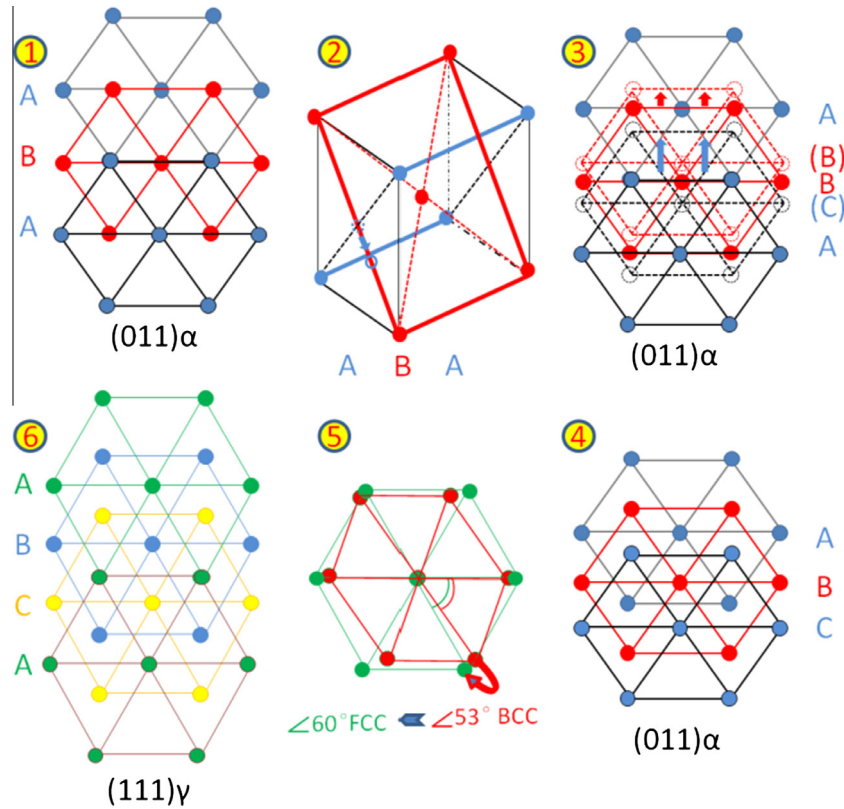


**Fig. 3.** Atomic correspondences for variants of reverse austenite phase with K–S orientation relationship with martensite phase. From ① to ⑥ shows how the body-centered-cubic atom stacking of martensite transforms to the face-centered-cubic atom stacking of austenite. Arrows in ②, ③, and ⑤ represent the atomic movement. The dots of the same color mean the same atom plane. (For interpretation of the references to color in this figure legend, the reader is referred to the web version of this article.)

**Table 1**

Grouping 24 K–S orientation relations into 3 Bain groups for FCC to BCC transformation.

K–S variants	FCC planes	BCC planes	FCC directions	BCC directions	Bain group
KS1	(1 1 1)	(0 1 1)	$[0 \bar{1} 1]$	$[1 \bar{1} 1]$	Z
KS2	(1 1 1)	(0 1 1)	$[0 \bar{1} 1]$	$[1 1 \bar{1}]$	Y
KS3	(1 1 1)	(0 1 1)	$[1 0 \bar{1}]$	$[1 \bar{1} 1]$	X
KS4	(1 1 1)	(0 1 1)	$[1 0 \bar{1}]$	$[1 1 \bar{1}]$	Z
KS5	(1 1 1)	(0 1 1)	$[\bar{1} 1 0]$	$[1 \bar{1} 1]$	Y
KS6	(1 1 1)	(0 1 1)	$[\bar{1} 1 0]$	$[1 1 \bar{1}]$	X
KS7	(1 $\bar{1}$ 1)	(0 1 1)	$[1 1 0]$	$[1 \bar{1} 1]$	X
KS8	(1 $\bar{1}$ 1)	(0 1 1)	$[1 1 0]$	$[1 1 \bar{1}]$	Y
KS9	(1 $\bar{1}$ 1)	(0 1 1)	$[\bar{1} 0 1]$	$[1 \bar{1} 1]$	Z
KS10	(1 $\bar{1}$ 1)	(0 1 1)	$[\bar{1} 0 1]$	$[1 1 \bar{1}]$	X
KS11	(1 $\bar{1}$ 1)	(0 1 1)	$[0 \bar{1} \bar{1}]$	$[1 \bar{1} 1]$	Y
KS12	(1 $\bar{1}$ 1)	(0 1 1)	$[0 \bar{1} \bar{1}]$	$[1 1 \bar{1}]$	Z
KS13	( $\bar{1} \bar{1} 1$ )	(0 1 1)	$[1 \bar{1} 0]$	$[1 \bar{1} 1]$	Y
KS14	( $\bar{1} \bar{1} 1$ )	(0 1 1)	$[1 \bar{1} 0]$	$[1 1 \bar{1}]$	X
KS15	( $\bar{1} \bar{1} 1$ )	(0 1 1)	$[0 1 1]$	$[1 \bar{1} 1]$	Z
KS16	( $\bar{1} \bar{1} 1$ )	(0 1 1)	$[0 1 1]$	$[1 1 \bar{1}]$	Y
KS17	( $\bar{1} \bar{1} 1$ )	(0 1 1)	$[\bar{1} 0 \bar{1}]$	$[1 \bar{1} 1]$	X
KS18	( $\bar{1} \bar{1} 1$ )	(0 1 1)	$[\bar{1} 0 \bar{1}]$	$[1 1 \bar{1}]$	Z
KS19	( $\bar{1} 1 1$ )	(0 1 1)	$[\bar{1} 1 0]$	$[1 \bar{1} 1]$	X
KS20	( $\bar{1} 1 1$ )	(0 1 1)	$[\bar{1} 1 0]$	$[1 1 \bar{1}]$	Y
KS21	( $\bar{1} 1 1$ )	(0 1 1)	$[1 0 1]$	$[1 \bar{1} 1]$	Z
KS22	( $\bar{1} 1 1$ )	(0 1 1)	$[1 0 1]$	$[1 1 \bar{1}]$	X
KS23	( $\bar{1} 1 1$ )	(0 1 1)	$[0 1 \bar{1}]$	$[1 \bar{1} 1]$	Y
KS24	( $\bar{1} 1 1$ )	(0 1 1)	$[0 1 \bar{1}]$	$[1 1 \bar{1}]$	Z

for instance, latent heat ( $Q$ ) for the transformation, and the under-cooling or overheating temperature  $\Delta T$  (difference between the cooling temperature or heating temperature and the equilibrium transformation temperature). In Eq. (2) we use a coupled free energy function to reflect the bulk free energy difference between

austenite and martensite phases in the transformation cycle. For each process, only one set of order parameters are involved. During martensitic transformation, the whole process is represented by the evolution of  $\{\eta_i\}$ , and in the following reverse transformation,  $\{\eta_i\}$  describe the initial morphology of martensite and the initial

**Table 2**  
Grouping 24 K–S orientation relations into 3 Bain groups for BCC to FCC transformation.

K–S variants	BCC planes	FCC planes	BCC directions	FCC direction	Bain group
KS1	(0 1 1)	(1 1 1)	[1 1 1]	[1 1 0]	Z
KS2	(0 1 1)	(1 1 1)	[1 1 1]	[1 0 1]	Z
KS3	(0 1 1)	(1 1 1)	[1 1 1̄]	[1 1 0]	Y
KS4	(0 1 1)	(1 1 1)	[1 1 1̄]	[1 0 1]	Y
KS5	(0 1̄ 1)	(1 1 1)	[1 1 1]	[1 1 0]	Z
KS6	(0 1̄ 1)	(1 1 1)	[1 1 1]	[1 0 1]	Z
KS7	(0 1̄ 1)	(1 1 1)	[1 1 1̄]	[1 1 0]	Y
KS8	(0 1̄ 1)	(1 1 1)	[1 1 1̄]	[1 0 1]	Y
KS9	(1 1̄ 0)	(1 1 1)	[1 1 1]	[1 1 0]	Y
KS10	(1 1̄ 0)	(1 1 1)	[1 1 1]	[1 0 1]	Y
KS11	(1 1 0)	(1 1 1)	[1 1 1]	[1 1 0]	X
KS12	(1 1 0)	(1 1 1)	[1 1 1]	[1 0 1]	X
KS13	(1 1 0)	(1 1 1)	[1 1 1]	[1 1 0]	X
KS14	(1 1 0)	(1 1 1)	[1 1 1]	[1 0 1]	X
KS15	(1 1 0)	(1 1 1)	[1 1 1]	[1 1 0]	Y
KS16	(1 1 0)	(1 1 1)	[1 1 1]	[1 0 1]	Y
KS17	(1̄ 1 0)	(1 1 1)	[1 1 1̄]	[1 1 0]	X
KS18	(1̄ 1 0)	(1 1 1)	[1 1 1̄]	[1 0 1]	X
KS19	(1̄ 1 0)	(1 1 1)	[1 1 1]	[1 1 0]	Z
KS20	(1̄ 1 0)	(1 1 1)	[1 1 1]	[1 0 1]	Z
KS21	(1 0 1)	(1 1 1)	[1 1 1]	[1 1 0]	Z
KS22	(1 0 1)	(1 1 1)	[1 1 1]	[1 0 1]	Z
KS23	(1 0 1)	(1 1 1)	[1 1 1̄]	[1 1 0]	X
KS24	(1 0 1)	(1 1 1)	[1 1 1̄]	[1 0 1]	X

stored energy distribution while the reverse transformation process is controlled by the evolution of  $\{\phi_j\}$ . The following is the specific local free energy function:

$$G_V^{local}(\{\eta_i\}, \{\phi_j\}, T) = G_V^0(\{\eta_i\}, \{\phi_j\}) + \Delta G(\{\eta_i\}, \{\phi_j\}, T) \quad (2)$$

where

$$G_V^0(\{\eta_i\}, \{\phi_j\}) = A \left( \sum_{i=1}^3 \eta_i^2 (\eta_i - 1)^2 + \sum_{j=1}^3 \phi_j^2 (\phi_j - 1)^2 \right) + A_\eta \sum_{i \neq j} \eta_i^2 \eta_j^2 + A_\phi \sum_{i \neq j} \phi_i^2 \phi_j^2 \quad (3)$$

is the local free energy at the equilibrium state with  $A$ ,  $A_\eta$ ,  $A_\phi$ , be the Landau coefficients [36,45–47].  $\Delta G(\{\eta_i\}, \{\phi_j\}, T)$  is the difference of Gibbs free energy between austenite and martensite at temperature  $T$ .

In the reverse transformation, defects in martensite are found to be the preferential nucleation sites of the reverse austenite [37,53]. Specifically, the growth of austenite is accompanied with the disappearance of defects. Thus, in this model, stored energy due to

defects is considered as a contribution of driving force for the reverse transformation. Fig. 4 illustrates the effect of stored energy on the thermodynamics of reverse austenitic transformation. The release of stored energy decreases the nucleation barrier of reverse austenite, and contributes to the driving force for the growth of reverse austenite. Therefore, we propose

$$\Delta G(\{\eta_i\}, \{\phi_j\}, T) = \left( \frac{Q(T - T_0)}{T_0} + G^{\text{defects}} \cdot \sum_{j=1}^3 \phi_j^2 \right) \cdot H(\{\eta_i\}, \{\phi_j\}) \quad (4a)$$

$$G^{\text{defects}} = r \cdot G^{\text{el}}(f \rightarrow b) \quad (4b)$$

where  $\sum_{j=1}^3 \phi_j^2$  is the shape function, and  $H(\{\eta_i\}, \{\phi_j\})$  is the interpolation function:

$$H(\{\eta_i\}, \{\phi_j\}) = B \left( \sum_{i=1}^3 (3\eta_i^2 - 2\eta_i^3) - \sum_{j=1}^3 (3\phi_j^2 - 2\phi_j^3) \right) \quad (5)$$

where  $B$  is the interpolation function coefficient. Eq. (4a) represents the decrease of bulk free energy during the cyclic transformation, and Eq. (4b) expresses the stored energy  $G^{\text{defects}}$  in the reverse transformation due to the formation of defects (e.g., dislocations) during the martensitic transformation process. The stored energy term characterizes the density of the generated defects. Typically, when the stress arising from phase transformations  $\sigma^{\text{trans}}$  exceeds the yield stress  $\sigma^Y$  of the material, the material is susceptible to the generation of defects, and the density of defects generated is proportional to the “exceeded” stress  $\sigma^{\text{trans}} - \sigma^Y$ ; moreover, by assuming that different martensitic variants have the same elastic properties,  $\sigma^{\text{trans}}$  is proportional to the transformation induced strain energy  $G^{\text{el}}(f \rightarrow b)$ . Therefore, as the “exceeded” energy, the stored energy is proportional to the density of defects. It can be evaluated based on Eq. (4b), where  $r$  measures the ratio of the stored energy obtained from the yield curve of the material to the coherency strain energy  $G^{\text{el}}(f \rightarrow b)$  from the microelasticity theory. The coefficient  $r$  is no less than 0 where no plasticity is involved ( $\sigma^{\text{trans}} \leq \sigma^Y$ ) and is less than 1.

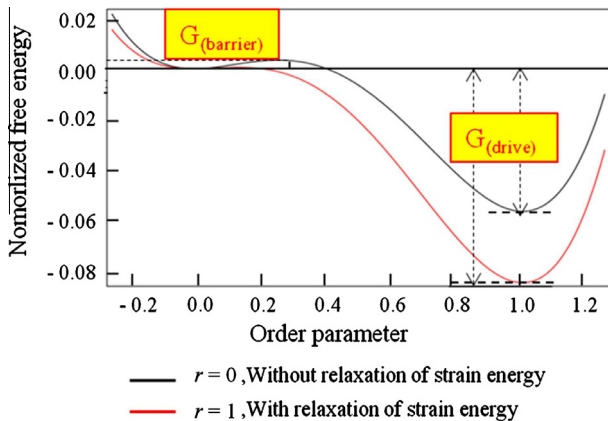


**Fig. 4.** Effects of stored energy from martensitic transformation on the thermodynamics of reverse austenitic transformation.

### 3.2. Coherency strain energy

As is discussed in Section 2, martensite and reverse austenite each has 24 different crystallographic variants, which can be divided into three groups. The coherency strain energy originated from the lattice mismatch during the displacive phase transformation plays a key role in the morphology of microstructures. From the microelasticity theory of Khachaturyan [36], the coherency strain energy density  $G_V^{el}$  Eq. (1) can be written as:

$$G_V^{el} = \frac{1}{2} C_{ijkl} \cdot \varepsilon_{ij}^{el} \cdot \varepsilon_{kl}^{el} \quad (6)$$

where  $C_{ijkl}$  is the elastic stiffness tensor and  $\varepsilon_{ij}^{el}$  is the elastic strain tensor. We assume that the elastic moduli are homogenous within the whole system.  $\varepsilon_{ij}^{el}$  is given by heterogeneous strain tensor  $\delta\varepsilon_{ij}$ , homogeneous strain tensor  $\bar{\varepsilon}_{ij}$  and eigenstrain tensor  $\varepsilon_{ij}^0$ , and the eigenstrain is determined by the lattice mismatch between new phase and parent phase. The elastic strain is calculated by:

$$\varepsilon_{ij}^{el} = \delta\varepsilon_{ij} + \bar{\varepsilon}_{ij} - \varepsilon_{ij}^0 \quad (7)$$

Eigenstrain  $\varepsilon_{ij}^0$  in this work is expressed by:

$$\varepsilon_{ij}^0 = \sum_{p=1}^3 \eta_p^2 \cdot \varepsilon_{ij}^0(f \rightarrow b)_p + \sum_{q=1}^3 \phi_q^2 \cdot \varepsilon_{ij}^0(b \rightarrow f)_q \quad (8)$$

taking both the eigenstrain of martensitic transformation,  $\varepsilon_{ij}^0(f \rightarrow b)$ , and the eigenstrain of reverse austenitic transformation,  $\varepsilon_{ij}^0(b \rightarrow f)$ , into consideration. They are coupled by interpolation functions  $\sum_{i=1}^3 \eta_i^2$  and  $\sum_{i=1}^3 \phi_i^2$ .

In Section 2 we get the “transformation matrix” for each of the martensite variants and reverse austenite variants (see [Supplementary materials](#)). As pointed out by Khachaturyan [36], we can get the transformation strain  $E_{(f \rightarrow b)}$  and  $E_{(b \rightarrow f)}$  and the principal axes of transformation strain through the “transformation matrix” [41]. Thus

$$\varepsilon_{ij}^0(f \rightarrow b) = E_{(f \rightarrow b)} = e_{(f \rightarrow b)} \cdot |\mathbf{M}| \cdot e_{(f \rightarrow b)}^{-1} - \mathbf{I} \quad (9a)$$

$$\varepsilon_{ij}^0(b \rightarrow f) = E_{(b \rightarrow f)} = e_{(b \rightarrow f)} \cdot |\mathbf{T}| \cdot e_{(b \rightarrow f)}^{-1} - \mathbf{I} \quad (9b)$$

where  $e_{(f \rightarrow b)}$  and  $e_{(b \rightarrow f)}$  are matrices composed of the principal transformation axes vectors for martensitic transformation and reverse transformation, respectively.  $|\mathbf{M}|$  and  $|\mathbf{T}|$  are diagonal matrices whose elements are the eigenvalues of square of the “Transformation Matrix”,  $\mathbf{M}^2$  and  $\mathbf{T}^2$  respectively (see [Supplementary materials](#)), and  $\mathbf{I}$  is the identity matrix. We get the eigenstrain for each of the variants groups as follows.

For martensitic transformation:

$$\begin{aligned} \varepsilon_{ij}^0(f \rightarrow b)_1 &= \begin{pmatrix} \varepsilon_1 & 0 & 0 \\ 0 & \varepsilon_1 & 0 \\ 0 & 0 & \varepsilon_3 \end{pmatrix} \\ \varepsilon_{ij}^0(f \rightarrow b)_2 &= \begin{pmatrix} \varepsilon_1 & 0 & 0 \\ 0 & \varepsilon_3 & 0 \\ 0 & 0 & \varepsilon_1 \end{pmatrix} \\ \varepsilon_{ij}^0(f \rightarrow b)_3 &= \begin{pmatrix} \varepsilon_3 & 0 & 0 \\ 0 & \varepsilon_1 & 0 \\ 0 & 0 & \varepsilon_1 \end{pmatrix} \end{aligned} \quad (10)$$

where  $\varepsilon_1 = 0.136$ ,  $\varepsilon_3 = -0.196$ . Here we ignore the rotation part, because it is relatively small according to the [Supplementary materials](#) [41]. The orthogonal strains are applied in our simulation.

For reverse austenitic transformation:

$$\begin{aligned} \varepsilon_{ij}^0(b \rightarrow f)_1 &= \begin{pmatrix} \varepsilon_1 & 0 & 0 \\ 0 & \varepsilon_1 & 0 \\ 0 & 0 & \varepsilon_3 \end{pmatrix} \\ \varepsilon_{ij}^0(b \rightarrow f)_2 &= \begin{pmatrix} \varepsilon_1 & 0 & 0 \\ 0 & \varepsilon_3 & 0 \\ 0 & 0 & \varepsilon_1 \end{pmatrix} \\ \varepsilon_{ij}^0(b \rightarrow f)_3 &= \begin{pmatrix} \varepsilon_3 & 0 & 0 \\ 0 & \varepsilon_1 & 0 \\ 0 & 0 & \varepsilon_1 \end{pmatrix} \end{aligned} \quad (11)$$

where  $\varepsilon_1 = -0.093$ ,  $\varepsilon_3 = 0.126$ .

### 3.3. Gradient energy

Gradient energy describes the energy penalty due to the inhomogeneous distribution of phase-field variables near interfaces [36,47–49]. In this work, it is only related to the inhomogeneity of structure order parameters near interfaces. The gradient energy can then be written as:

$$\begin{aligned} G_V^{grad}(\{\nabla \eta_i\}, \{\nabla \phi_j\}) &= \frac{1}{2} \sum_{i=1}^3 k_{\eta,pq}^0 (\nabla_p \eta_i) (\nabla_q \eta_i) \\ &+ \frac{1}{2} \sum_{j=1}^3 k_{\phi,pq}^0 (\nabla_p \phi_j) (\nabla_q \phi_j) \end{aligned} \quad (12)$$

$k_{\eta,pq}^0$  and  $k_{\phi,pq}^0$  are the gradient coefficients matrices and both are considered isotropic.

### 3.4. Governing equations

The microstructure evolution is governed by the free energy minimizing process. Since there is no diffusional process during the cyclic transformation, the Allen–Cahn (time-dependent Ginzburg–Landau) equation governs the kinetics of structural phase transformation [32]:

$$\frac{\partial \eta_i(r, t)}{\partial t} = - \sum_{i=1}^3 L_{ij} \cdot \frac{\delta G_{total}}{\delta \eta_j} \quad (13a)$$

$$\frac{\partial \phi_p(r, t)}{\partial t} = - \sum_{p=1}^3 L_{pq} \cdot \frac{\delta G_{total}}{\delta \phi_q} \quad (13b)$$

where Eqs. (13a) and (13b) represent the microstructural evolution of martensitic transformation and reverse austenitic transformation respectively.  $L_{ij}$  and  $L_{pq}$  are the kinetic coefficients and they are both considered isotropic [31,43,44].

## 4. Computer simulations and discussions

### 4.1. Numerical input data

The governing equations Eqs. (13a) and (13b) were solved in dimensionless unit, thus all the parameters should be normalized:  $\Delta x^* = \frac{\Delta x}{l}$ ,  $\Delta t^* = L \cdot E \cdot \Delta t$ ,  $G^* = \frac{G}{E}$ ,  $C_{ij}^* = \frac{C_{ij}}{E}$ ,  $k^* = \frac{k}{E \cdot l^2}$ , where  $E$  is the characteristic energy, chosen to be  $10^9$  J/m<sup>3</sup>, and  $l$  is the characteristic length, chosen to be  $10^{-9}$  m.  $\Delta x$  and  $\Delta t$  are the discretization grid size and time step respectively. We employed uniform grids, i.e.,  $\Delta x = \Delta y = \Delta z$ .  $\Delta x^*$  was chosen to be 0.5, and  $\Delta t^*$  was chosen to be 0.025 during the nucleation steps and 0.1 afterwards. For each simulation, Langevin noise terms were added during the first 100 simulation steps to simulate the nucleation process and avoid any *a priori* assumptions on microstructures. During the martensitic transformation process we chose the elastic moduli of *fcc*

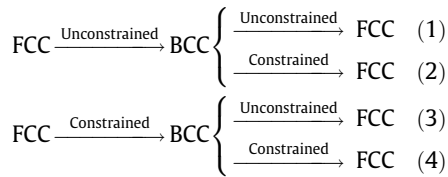
**Table 3**  
Non-dimensionalized parameters in phase-field simulations.

Parameters	Values	Parameters	Values
$A^*$	0.2	$C_{11,bcc}^*$	70.86
$A_\eta^*$	5.0	$C_{12,bcc}^*$	31.43
$A_\phi^*$	5.0	$C_{44,bcc}^*$	34.29
$A_{\eta,\phi}^*$	0.25	$C_{11,fcc}^*$	59.71
$Q^*$	0.35	$C_{12,fcc}^*$	38.0
$(k_{\eta,pq}^0)^*$	0.1	$C_{44,fcc}^*$	34.57
$(k_{\phi,pq}^0)^*$	0.1	$\Delta x^* = \Delta y^* = \Delta z^*$	0.5

Fe–Ni for the entire system [50], and the elastic moduli of bcc Fe–Ni [50] for the entire system in reverse austenitic phase transformation. The simulations were conducted in a  $128\Delta x \times 128\Delta x \times 128\Delta x$  3D system. The non-dimensionalized parameters are tabulated in Table 3. In the simulation of martensitic transformation, we chose  $T = 300$  K, which is lower than  $M_s = 435$  K, and  $T = 820$  K for simulation of reverse austenitic transformation which is higher than  $A_s = 793$  K and lower than  $A_f = 853$  K of Fe–23Ni [37].

#### 4.2. Microstructure evolution

Effects of phase-transformation-induced strain energy and stored energy on reverse transformation are investigated by phase-field simulations under different mechanical boundary conditions with different initial states. These energy factors behave differently under different boundary conditions to affect the microstructure morphology and kinetics of the phase transformations, which are important indicators of the austenite memory effect. Specifically, the austenite memory effect is related to the evolution of the size of the austenite, and we are especially interested in the final microstructure morphology of the reverse austenite, whether or not it will integrate into coarse austenite grains to display the “austenite memory” phenomenon. Therefore, we investigate the morphology and kinetics of microstructure evolution for four kinds of simulation paths as follows:



In these cases, the stored energy obtained from the FCC to BCC transformation is kept as the initial condition of the following BCC to FCC transformation with the change of the mechanical boundary condition. This means the source of the stored energy is the generated structural defects during the martensitic transformation.

Different mechanical boundary conditions of the system have different effects on the elastic energy distributions during a phase transformation, and will affect the nucleation and growth kinetics, as well as the final morphologies, of the phase transformation. Here we briefly discuss the difference between the unconstrained (stress free) and constrained (strain free) boundary conditions. According to the microelasticity theory [36], the elastic strain energy of a system undergoing phase transformations is

$$E^{el} = \frac{1}{2} \int C_{ijkl} (\delta \varepsilon_{ij}(\mathbf{r}) + \bar{\varepsilon}_{ij} - \varepsilon_{ij}^0(\mathbf{r})) (\delta \varepsilon_{kl}(\mathbf{r}) + \bar{\varepsilon}_{kl} - \varepsilon_{kl}^0(\mathbf{r})) d^3 \mathbf{r} \quad (14)$$

Since the heterogeneous strain  $\delta \varepsilon_{ij}(\mathbf{r})$  would not cause the macroscopic shape change,  $\int \delta \varepsilon_{ij}(\mathbf{r}) d^3 \mathbf{r} = 0$ . Moreover, the eigenstrain  $\varepsilon_{ij}^0(\mathbf{r})$  can be written as  $\varepsilon_{ij}^0(\mathbf{r}) = \sum_p \varepsilon_{ij}^0(p) \cdot \theta_p(\mathbf{r})$  where  $\varepsilon_{ij}^0(p)$  is the

stress-free transformation strain of the  $p$ -th variant of the product phase (e.g.,  $\varepsilon_{ij}^0(f \rightarrow b)$  in Eq. (8)) and  $\theta_p(\mathbf{r})$  is the shape function of the  $p$ -th variant (e.g.,  $\eta_p^2$  in Eq. (8)). The shape function  $\theta_p(\mathbf{r})$  satisfies  $\int \theta_p(\mathbf{r}) d^3 \mathbf{r} = V_p$  where  $V_p$  is the volume of the  $p$ -th variant. With these constraints, by calculating Eq. (14), we get

$$\begin{aligned} E^{el} = & \frac{V}{2} C_{ijkl} \bar{\varepsilon}_{ij} \bar{\varepsilon}_{kl} - \sum_p V_p C_{ijkl} \bar{\varepsilon}_{ij} \varepsilon_{kl}^0(p) + \sum_p \frac{V_p}{2} C_{ijkl} \varepsilon_{ij}^0(p) \varepsilon_{kl}^0(p) \\ & + \int \left( \frac{1}{2} C_{ijkl} \delta \varepsilon_{ij}(\mathbf{r}) \delta \varepsilon_{kl}(\mathbf{r}) - C_{ijkl} \delta \varepsilon_{ij}(\mathbf{r}) \varepsilon_{kl}^0(\mathbf{r}) \right) d\mathbf{r}^3 \quad (15) \end{aligned}$$

where  $V$  is the volume of the whole system. The difference of unconstrained and constrained boundary conditions lies in the values of homogeneous strain  $\bar{\varepsilon}_{ij}$ . Under constrained boundary condition, since the volume and shape of the entire system are fixed to the initial states,  $\bar{\varepsilon}_{ij} = 0$ , and therefore the first two terms in Eq. (15) related to  $\bar{\varepsilon}_{ij}$  are zero. On the other hand, under unconstrained boundary condition, the elastic energy is minimized with respect to the homogeneous strain  $\bar{\varepsilon}_{ij}$ , i.e.,  $\frac{\partial E^{el}}{\partial \bar{\varepsilon}_{ij}} = 0$ , from which we obtain  $\bar{\varepsilon}_{ij} = \sum_p \frac{V_p}{V} \varepsilon_{ij}^0(p)$ . Assuming the product phase has the same configurations and spatial distributions under unconstrained and constrained boundary conditions, by comparing the first two terms in Eq. (15), we have:

$$\begin{aligned} E_{ex}^{el} = & E_{constrained}^{el} - E_{unconstrained}^{el} \\ = & 0 - \left( -\frac{V}{2} C_{ijkl} \left( \sum_p \frac{V_p}{V} \varepsilon_{ij}^0(p) \right) \left( \sum_p \frac{V_p}{V} \varepsilon_{kl}^0(p) \right) \right) \\ = & \frac{V}{2} C_{ijkl} \left( \sum_p \frac{V_p}{V} \varepsilon_{ij}^0(p) \right) \left( \sum_p \frac{V_p}{V} \varepsilon_{kl}^0(p) \right) \quad (16) \end{aligned}$$

Eq. (16) gives the additional elastic strain energy under constrained boundary condition than under unconstrained boundary condition. Since the elastic energy in Eq. (16) is related to the volume fraction  $V_p/V$  of each variant of the product phase, it will influence the kinetics of the whole transformation process, i.e., increasing the nucleation barrier and decreasing the driving force for growth. As a result, there will be a decrease in both nucleation sites and growth rates for the new phase. Moreover, to minimize the elastic energy in Eq. (16), different variants of the product phase will arrange themselves in such a way that  $\sum_p \frac{V_p}{V} \varepsilon_{ij}^0(p)$  is minimized. This may lead to self-accommodation of certain variants so that the variants have the same volume fraction and  $\sum_p \frac{V_p}{V} \varepsilon_{ij}^0(p)$  is minimized, or even the suppression of the phase transformation ( $V_p = 0$  or very small) when the elastic energy is too large.

##### 4.2.1. Martensitic transformation under different mechanical boundary conditions

In this work, like that in the experiments [51,52], solution treatment (heating to high temperature (1473 K), holding for hours and then “water-quenching” to room temperature) is first conducted to get the initial martensite structure. Thus phase-field simulations of martensitic transformation under unconstrained and constrained boundary conditions are conducted. In the simulation of martensitic transformation under unconstrained boundary condition, one of the martensite variants tends to occupy the whole system, thus provides the absolute minimum of the free energy for the whole system as long as the simulation steps are long enough [33]. Fig. 5(a)–(d) shows the microstructural evolution of lath martensite; in Fig. 5(d) variant 2 has a larger volume fraction than variant 3, Fig. 5(e) is the sectional view in (d) marked by the white dashed lines. Fig. 5(f) shows the distribution of normalized elastic energy along the black dashed line in (e), indicating that

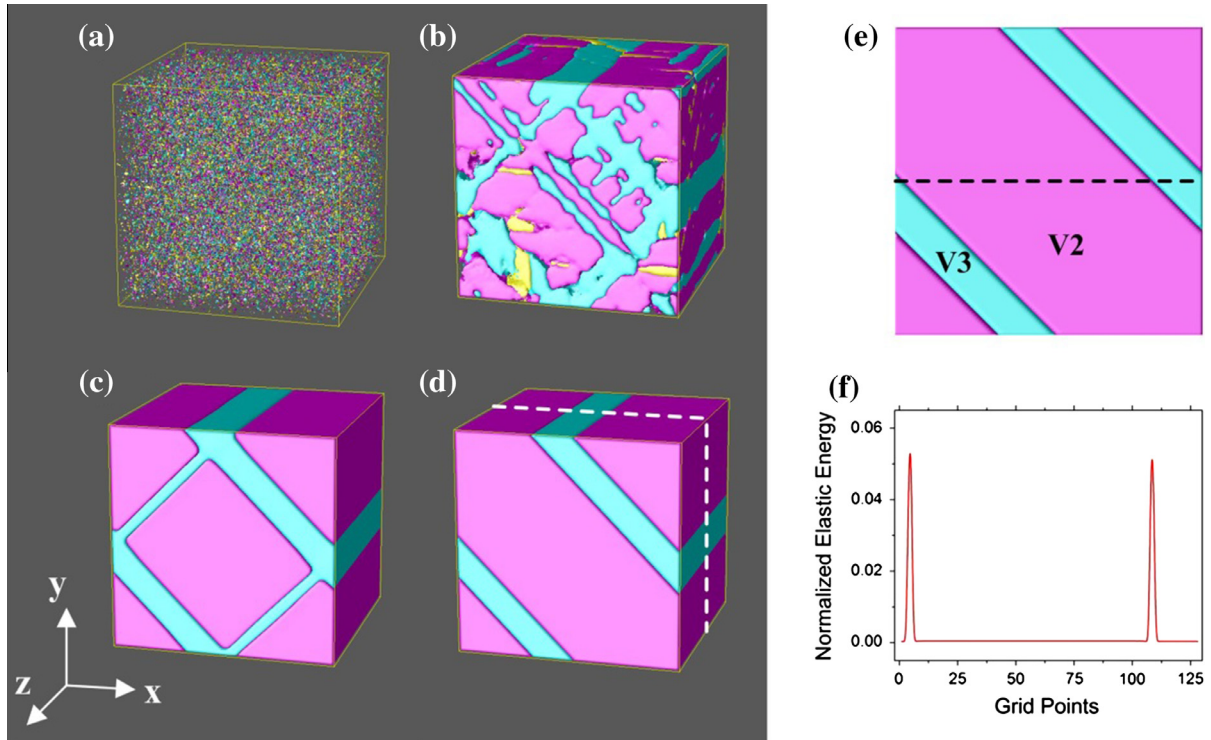


**Fig. 5.** From (a) to (d) shows the microstructural evolution of martensitic transformation under unconstrained boundary condition. V2 and V3 are two of the three Bain variants of martensite. (e) Is the sectional view in (d) marked by the white dashed lines, and (f) shows the distribution of normalized elastic energy along the black dashed line in (e).

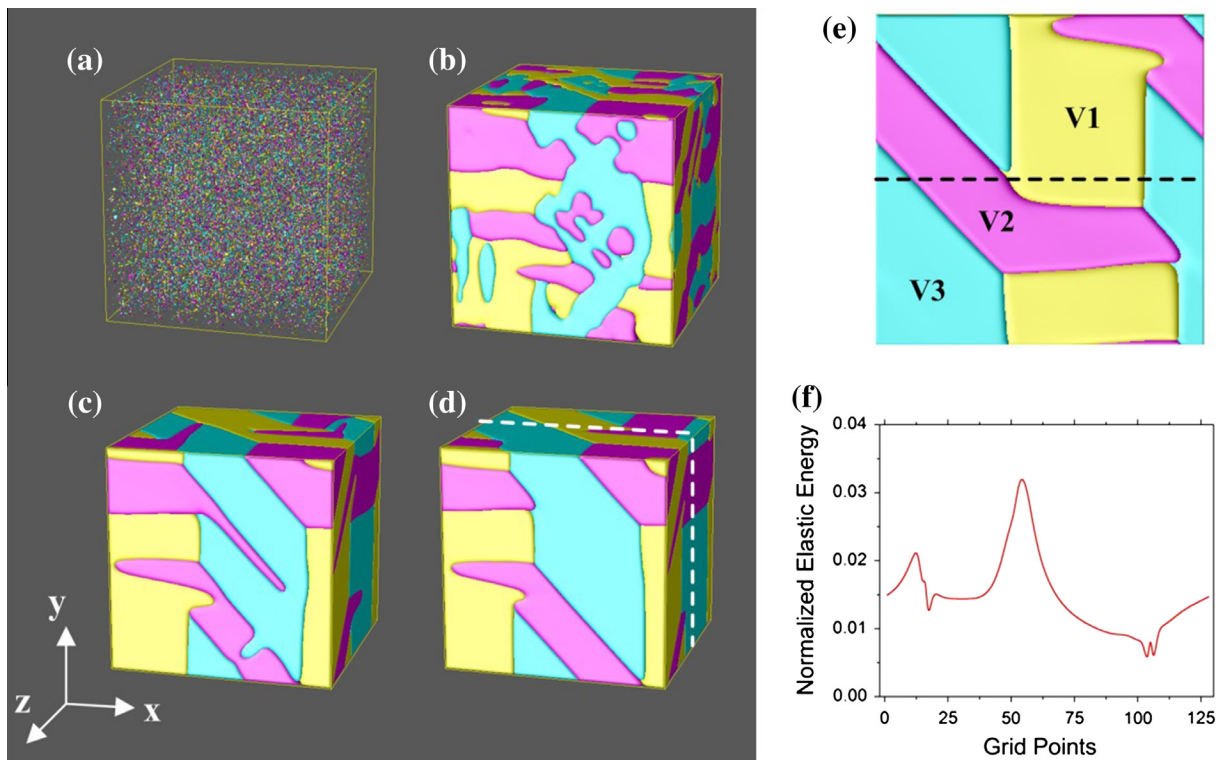


**Fig. 6.** From (a) to (d) shows the microstructural evolution of martensitic transformation under constrained boundary condition. V1, V2 and V3 are the three Bain variants of martensite. (e) Is the sectional view in (d) marked by the white dashed lines, and (f) shows the distribution of normalized elastic energy along the black dashed line in (e).

the phase-transformation-induced strain energy exists only at the lath boundaries, which also reflects the distribution of stored energy, since we assume that the stored energy is proportional to phase

transformation induced strain energy (Eq. (4b)). Without any constraint, the phase-transformation-induced stress can be largely released through the volume and shape change of the new phase.

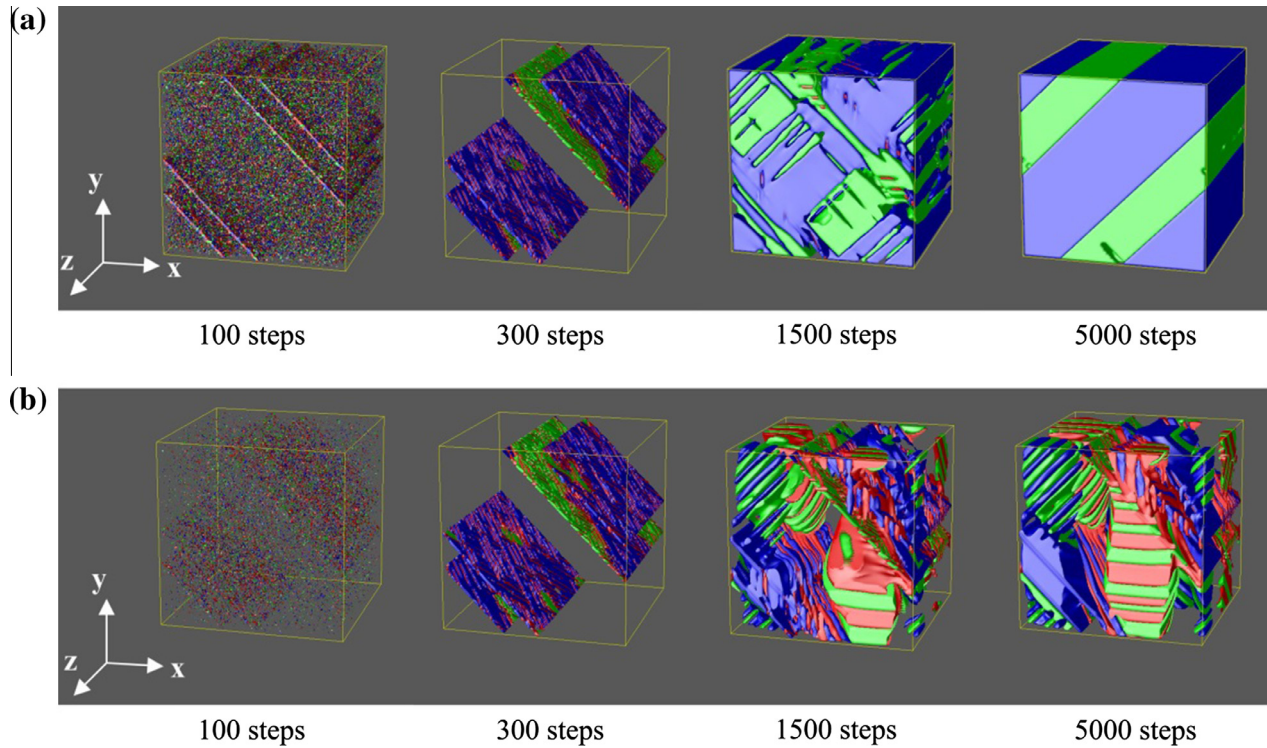


**Fig. 7.** Microstructural evolution of reverse austenitic transformation starting from unconstrained martensite, with (a) unconstrained boundary condition (b) constrained boundary condition. The red, green and blue colors represent the three Bain variants of the austenite. (For interpretation of the references to color in this figure legend, the reader is referred to the web version of this article.)

Simulation of martensitic transformation under constrained condition is another way to prepare the initial martensite (morphology and stored energy distribution) for reverse transformation. From Fig. 6 we get the microstructural evolution and the stored energy distribution. In Fig. 6(a)–(d), typical martensitic lath morphology consisting of twin-related variants is similar to that in Fig. 5; moreover, variant 1 also exists and has a twin-relationship with variant 2 and variant 3. Fig. 6(e) is the sectional view in Fig. 6(d) marked by the white dashed lines. Under constrained boundary condition, all of the Bain variants exist to reduce the strain energy of the whole system through strain accommodation, *i.e.*, different variants coexist to relax the phase-transformation-induced strain energy as much as possible [33], due to the additional elastic strain energy in Eq. (16). The distributions and the relative values of the stored energy are also different from that under unconstrained condition, as compared from Figs. 5(f) and 6(f). It is larger at the lath boundaries than inside the laths, and it is much larger at the triple-point of variant 1, 2 and 3, in Fig. 6(f). In contrast to Fig. 5(f), the elastic strain energy in Fig. 6(f), and therefore stored energy, distributes all over the system, providing more nucleation sites for the reverse austenitic transformations.

#### 4.2.2. Reverse austenitic transformations

**4.2.2.1. Reverse transformation from unconstrained martensite to austenite.** In this simulation we take the result from the unconstrained martensite simulations (Fig. 5) as the initial states of the reverse austenitic transformation. Under the unconstrained boundary condition, the reverse austenite nucleates and grows along lath boundaries at the beginning of transformation; after that, the nuclei proceed inward and finally integrate into a larger reverse austenite lath, leading to the “austenite memory” phenomenon. Fig. 7(a) shows this whole process and it matches the experimental results quite well [37,52,53]. From the former simu-

lations in Section 4.2.1, stored energy at lath boundaries is much higher than that inside martensite laths. Therefore, at lath boundaries the available nucleation sites and driving force for the growth of the reverse austenite is higher than that inside laths. This can be an important reason for the preferential nucleation and growth behavior at martensite lath boundaries of reverse austenite.

Under constrained condition (Fig. 7(b)), the nucleation behavior is similar to that under unconstrained boundary condition: austenite nucleates at lath boundaries, because of the same reason as that in Fig. 7(a). However, the growth of austenite is much slower than that in Fig. 7(a), primarily due to the additional strain energy in Eq. (16) during transformation process, which decreases the driving force of phase transformation and thus delays the evolution of reverse austenite, as has been stated by Eqs. (14)–(16). Consequently, the “austenite memory” phenomenon is suppressed and the reverse austenitic phase transformation is incomplete even after 5000 simulation steps (*i.e.*, certain amount of martensite is retained) due to the large strain energy induced by phase transformations.

**4.2.2.2. Reverse transformation from constrained martensite to austenite.** This simulation is conducted with an initial state of constrained martensite. As displayed in Fig. 8(a), under the unconstrained condition, the reverse austenite tends to nucleate at both the lath boundaries and inside the martensite laths. After nucleation, to reduce the strain energy induced by reverse austenitic transformation, the reverse austenite nuclei grow into different orientation variants, and meet each other to form larger variants or twin-related variant couples. Comparing with the simulations starting from unconstrained martensite in Section 4.2.2.1, transformation at early stages ( $\sim 300$  simulation steps) in this simulation evolves much faster. Meanwhile, the size of reverse austenite laths in Fig. 8(a) is smaller than that in Fig. 7(a), which is in agreement with the conclusion from experiments that reverse austenite

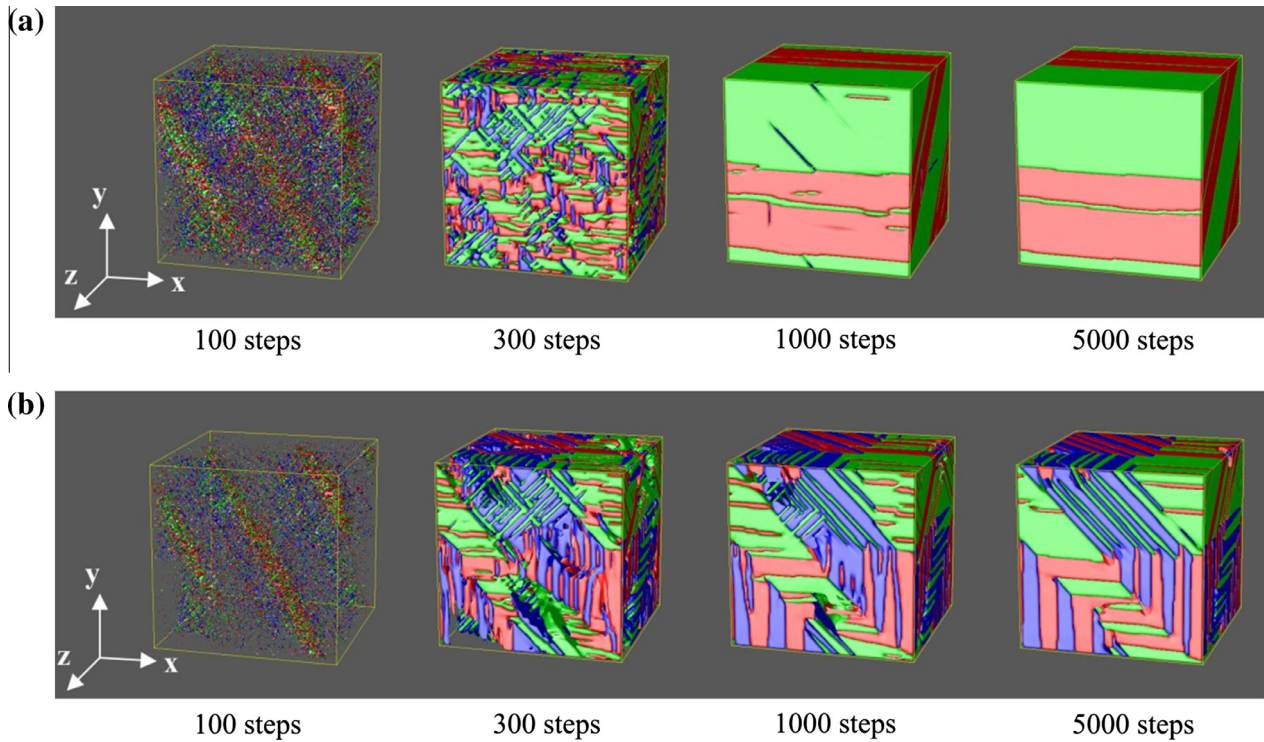


**Fig. 8.** Microstructural evolution of reverse austenitic transformation starting from constrained martensite, with (a) unconstrained boundary condition (b) constrained boundary condition. The red, green and blue colors represent the three Bain variants of the austenite. (For interpretation of the references to color in this figure legend, the reader is referred to the web version of this article.)

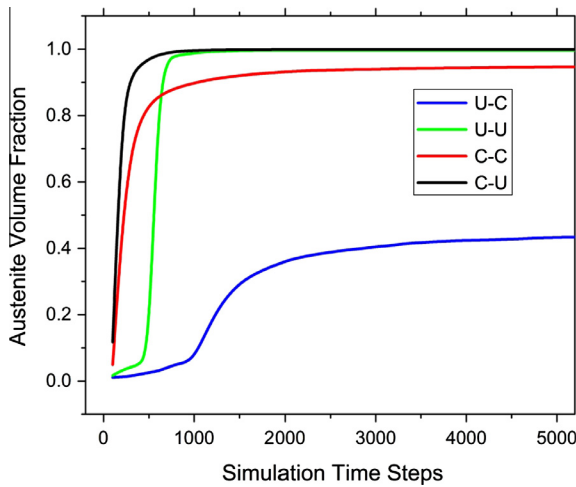


**Fig. 9.** Kinetics of reverse austenitic transformations. U-U: starting from unconstrained martensite and evolving under unconstrained boundary condition; U-C: starting from unconstrained martensite and evolving under constrained boundary condition; C-U: starting from constrained martensite and evolving under unconstrained boundary condition; C-C: starting from constrained martensite and evolving under constrained boundary condition.

nucleating inside martensite laths tends to form small size variants [53]. This is primarily due to the more even distribution of the stored energy within the initial constrained martensite. Although the stored energy is still higher at martensite lath boundaries (Fig. 6(f)), the stored energy inside laths of constrained martensite is much higher than that inside unconstrained martensite, which enables nucleation of reverse austenite inside the martensite laths. As a result, there are more preferential nucleation sites for reverse austenite in constrained martensite, leading to the refined austenite laths during early stages of the transformation. However, if we

simulate the process for even longer time (e.g., 5000 simulation steps in Fig. 8(a)), which mimics holding the sample at high temperatures for enough long time, smaller austenite laths integrate into larger laths, which leads to the “austenite memory” phenomenon. This is mainly due to the effect of unconstrained boundary condition during the reverse austenitic transformation, in which the phase-transformation-induced stress can be largely released through the volume and shape change of the new phase, so that the whole system tends to form a single reverse austenite variant to reduce the elastic and interfacial energies.

In Fig. 8(b), under constrained condition, the microstructure evolution of reverse austenite is similar to that in Fig. 8(a) at the austenite nucleation process, but the growth behavior is quite different. The size of the reverse austenite remains smaller, since all the three variants tend to coexist to reduce the strain energy, which mitigates the “austenite memory” effect. Indeed, based on the simulation results for all the four sets of transformation paths with different mechanical boundary conditions, reverse transformations with constrained boundary condition result in the finest austenite variants, which best mitigates the austenite memory effect. On the other hand, the unconstrained boundary condition will promote the austenite memory effect. In addition to the morphology difference, the transformation rate is lower under constrained boundary condition. The growth behavior is affected by both the strain energy induced by the martensitic transformation and the strain energy induced by the reverse austenitic transformation.

#### 4.2.3. Kinetics of reverse austenitic transformation under different conditions

As discussed above, different mechanical boundary conditions have different effects on thermodynamics and kinetics of phase transformation. Furthermore, these effects are directly related to microstructure evolution. Fig. 9 shows the fraction of reverse

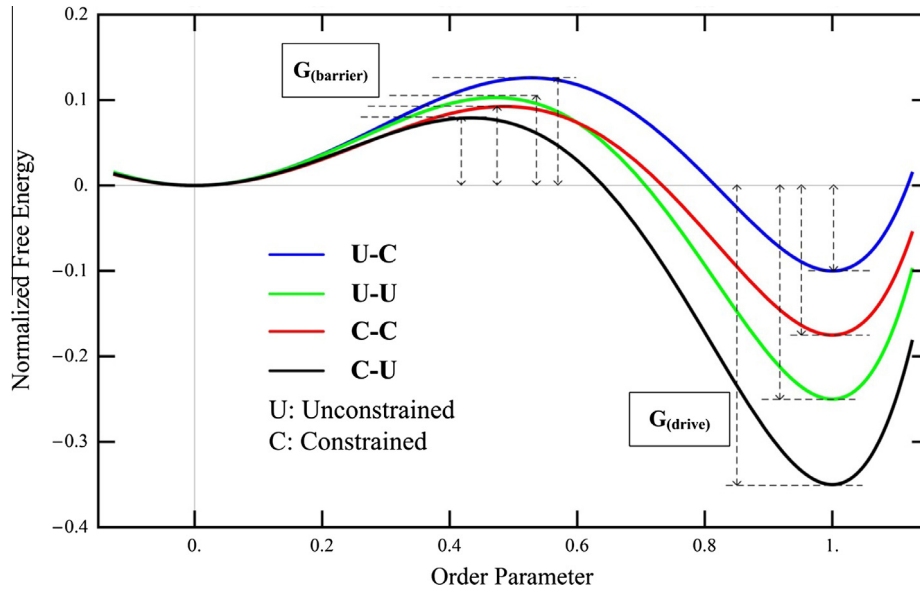


**Fig. 10.** Effect of boundary conditions on thermodynamics of reverse transformation.  $G_{(\text{barrier})}$ : the barrier energy of reverse austenite nucleation;  $G_{(\text{drive})}$ : the driving force of reverse austenite growth. The symbols of “U–U”, “U–C”, “C–U” and “C–C” have the same meaning as those in Fig. 9.

austenite with respect to modeling time steps. Comparing the austenite fractions of the four simulation paths during the initial nucleation stages (*i.e.*, simulation steps less than 500), their corresponding transformation (or nucleation) rates have the relationship of: “C–U” > “C–C” > “U–U” > “U–C”. Here U represents unconstrained boundary condition, and C represents constrained boundary condition. Thus, U–U means simulation starts from unconstrained martensite and evolves under unconstrained boundary condition. U–C, C–U and C–C have similar meaning. This result indicates the significant effect of the first mechanical boundary condition (*i.e.*, the mechanical boundary condition during the martensitic transformation), due to the difference of the distribution and relative values of the stored energy, on the nucleation behavior of the reverse austenite. For reverse austenitic transformations starting from constrained martensite, since the stored energy distributes within the whole system, and the values are relatively high (much higher than that inside the unconstrained martensite laths), there are more possible nucleation sites for reverse austenite in the constrained martensite than in the unconstrained martensite, leading to the faster nucleation. Moreover, during the subsequent growth stages of the reverse austenite (*i.e.*, simulation steps larger than 500), “U–U” gradually wins over “C–C” in austenite fraction, since the second mechanical boundary condition (*i.e.*, the mechanical boundary condition during the reverse austenitic transformation) plays a key role in the growth rate of the reverse austenite, as discussed in Section 4.2. Finally, the reverse austenitic transformations under unconstrained boundary conditions (“C–U” and “U–U”) end much faster than those under constrained boundary conditions (“C–C” and “U–C”).

Based on the observations above, Fig. 10 summarizes the interplay of the stored energy and the elastic strain energy for the austenite growth behaviors under different combinations of the mechanical boundary conditions during the  $\gamma \rightarrow \alpha \rightarrow \gamma$  transformation cycle. As illustrated, “U–C” has the highest nucleation barrier and the lowest driving force for growth, due to the limited nucleation sites provided by the stored energy from the martensitic transformation and the presence of the additional elastic energy of Eq. (16) during the reverse austenitic transformation. On the contrary, “C–U” has the lowest energy barrier and the highest driving force for growth, since the stored energy and the absence of the additional elastic energy of Eq. (16) both promote the transforma-

tion. In addition, “C–C” has lower nucleation barrier than “U–U” but lower driving force for growth than “U–U”.

Based on the discussions above, the mitigation of the “austenite memory” phenomenon in the “U–C” and “C–C” path is realized by the suppression of the growth rate of the reverse austenite. Comparing “U–C” and “C–C”, the “C–C” path has more nucleation sites for the reverse austenite, which leads to the faster growth rate and completion of the reverse transformation. The “U–C” path, with fewer nucleation sites and less growth driving force, suppresses the reverse austenite to a large extent. Both “C–C” and “U–C” can be the desirable path in terms of mitigating the austenite memory phenomenon. Especially, the generation of more nucleation sites and suppression of growth rates through the manipulation of mechanical boundary conditions could be a reasonable guidance for experiments to get smaller austenite grains during the reverse transformation.

## 5. Conclusion

In this work, to study the “austenite memory” phenomenon during the reverse austenitic transformation in Fe–23Ni (wt.%), we first assume the displacive nature of the martensite  $\rightarrow$  austenite transformation, and derive the corresponding transformation strains based on the crystallographical theory [36]. We then, by introducing the “stored energy” to consider the effects of defects generated in martensitic transformation on the reverse austenitic transformation, apply the phase-field method to simulate the microstructure evolution of the reverse austenitic transformation under different mechanical boundary conditions. Using the morphology of the austenite variants, whether or not they will integrate into coarse ones, as the criterion, the “austenite memory” phenomenon is discussed for the simulation results. Based on the discussions, the following conclusions can be drawn:

- (1) The “C–C” and “U–C” simulation paths can both eliminate the “austenite memory” phenomenon. Especially, the “C–C” path generates more nucleation sites for the reverse austenite through the constrained boundary condition during the prior martensitic transformation and suppresses the growth rate of the reverse austenite through the constrained boundary condition during the reverse austenitic transformation.

- (2) The effect of the mechanical boundary conditions of the prior martensitic transformation lies in the inhomogeneous distribution of the stored energy generated by defects during the martensitic transformation, which primarily decreases the nucleation barrier and provides nucleation sites for the reverse austenite.
- (3) The effect of the mechanical boundary conditions of the reverse austenitic transformation lies in the difference in the transformation-induced strain energy, which primarily decreases the driving force of the growth of the reverse austenite.

These insights can provide useful guidance for experiments to mitigate the austenite memory effect and get smaller austenite grain during the reverse austenitic transformations.

### Acknowledgments

This work was supported by financial support from the National Natural Science Foundation of China (No. 51171087), and from the National Basic Research Program of China (Nos. 2015GB118000 and 2015CB654802). The computer simulations were carried out on the LION clusters at the Pennsylvania State University.

### Appendix A. Supplementary data

Supplementary data associated with this article can be found, in the online version, at <http://dx.doi.org/10.1016/j.commatsci.2016.01.030>.

### References

- [1] T. Maki, *Mater. Sci. Forum.* 56–58 (1990) 157–168.
- [2] S. Morito, H. Saito, T. Ogawa, T. Furuhashi, T. Maki, *ISIJ Int.* 45 (2005) 91–94.
- [3] S. Morito, H. Yoshida, T. Maki, X. Huang, *Mater. Sci. Eng. A* 438–440 (2006) 237–240.
- [4] N. Tsuji, T. Maki, *Scripta Mater.* 60 (2009) 1044–1049.
- [5] T. Maki, *Mater. Sci. Forum.* 558–559 (2007) 23–31.
- [6] B.S. Altan (Ed.), *Severe Plastic Deformation toward Bulk Production of Nanostructured Materials*, NOVA Science Publishers, New York, 2005.
- [7] F. Masuyama, *ISIJ Int.* 41 (2001) 612–625.
- [8] A. Di Schino, M. Basteri, J.M. Kenny, *J. Mater. Sci. Lett.* 9 (2002) 751–753.
- [9] H. Shirazi, G. Miyamoto, S.H. Nedjad, H.G. Nanesa, M.N. Ahmadabadi, T. Furuhashi, *J. Alloys Compd.* 577 (2013) s572–s577.
- [10] V.D. Sadovskiy, *Structural Inheritance, Metallurgia*, Moscow, 1973.
- [11] A.S. Chaus, F.I. Rudnitskii, M. Murgas, *Met. Sci. Heat Treat.* 39 (1997) 53–56.
- [12] L.T. Zayats, D.O. Panov, M.G. Zakirova, *Met. Sci. Heat Treat.* 50 (2008) 473–477.
- [13] T. Hara, N. Maruyama, Y. Shinohara, H. Asahi, G. Shigesato, M. Sugiyama, T. Koseki, *ISIJ Int.* 49 (2009) 1792–1800.
- [14] S.T. Kimmmins, D.J. Gooch, *Met. Sci.* 17 (1983) 519–532.
- [15] L. Liu, Z.-G. Yang, C. Zhang, *J. Alloys Compd.* 577 (2013) S654–S660.
- [16] N. Nakada, T. Tsuchiyama, S. Takaki, S. Hashizume, *ISIJ Int.* 47 (2007) 1527.
- [17] V.V. Sagaradze, V.E. Danilchenko, Ph. L'Heritier, V.A. Shabashov, *Mater. Sci. Eng. A* 337 (2002) 146–159.
- [18] Y.K. Lee, H.C. Shin, D.S. Leem, J.Y. Choi, W. Jin, C.S. Choi, *Mater. Sci. Technol.* 19 (2003) 393–398.
- [19] K. Tomimura, S. Takaki, Y. Tokunga, *ISIJ Int.* 31 (1991) 1431–1437.
- [20] S.J. Lee, Y.M. Park, Y.K. Lee, *Mater. Sci. Eng. A* 515 (2009) 32–37.
- [21] D. Qiu, W.-Z. Zhang, *Acta Mater.* 55 (2007) 6754–6764.
- [22] S. Rajasekhara, P.J. Ferreira, *Acta Mater.* 59 (2011) 738–748.
- [23] F. Danoix, P. Auger, *Mater. Character.* 44 (2000) 177–201.
- [24] M. Mamivand, M.A. Zaeem, H.EI. Kadiri, *Comput. Mater. Sci.* 77 (2013) 304–311.
- [25] N. Moelans, B. Blanpain, P. Wollants, *Comput. Coupl. Phase Diag. Thermochem.* 32 (2008) 268–294.
- [26] M. Militzer, *Curr. Opin. Solid State Mater. Sci.* 15 (2011) 106–115.
- [27] L.Q. Chen, *Annu. Rev. Mater. Res.* 32 (2002) 113.
- [28] H.K. Yeddu, PhD Dissertation, KTH Royal Institute of Technology, 2012.
- [29] A. Artemev, Y. Wang, A.G. Khatchaturyan, *Acta Mater.* 48 (2000) 2503–2518.
- [30] H.K. Yeddu, V.I. Razumovskiy, A. Borgenstam, P.A. Korzhavyi, A.V. Ruban, J. Agren, *Acta Mater.* 60 (2012) 6508–6517.
- [31] H.K. Yeddu, A. Malik, J. Agren, G. Amberg, A. Borgenstam, *Acta Mater.* 60 (2012) 1538–1547.
- [32] Y. Wang, A.G. Khatchaturyan, *Acta Mater.* 45 (1997) 759–773.
- [33] A. Artemev, Y. Jin, A.G. Khatchaturyan, *Acta Mater.* 49 (2001) 1165–1177.
- [34] H.K. Yeddu, T. Lookman, A. Saxena, *J. Mater. Sci.* 49 (2014) 3642–3651.
- [35] A. Artemev, Y. Jin, A.G. Khatchaturyan, *Phil. Mag. A* 82 (2002) 1249.
- [36] A.G. Khatchaturyan, *Theory of Structural Transformations in Solids*, John Wiley & Sons, New York, 1983.
- [37] H. Shirazi, PhD Dissertation, The Tohoku University, 2013.
- [38] S.S. D'yachenko, *Met. Sci. Heat Treat.* 42 (2000) 122–127.
- [39] S. Morito, H. Tanaka, R. Konishi, T. Furuhashi, T. Maki, *Acta Mater.* 51 (2003) 1789–1799.
- [40] X.-F. Gu, W.-Z. Zhang, D. Qiu, *Acta Mater.* 59 (2011) 4944–4956.
- [41] Z. Guo, C.S. Lee, J.W. Morris Jr., *Acta Mater.* 52 (2004) 5511.
- [42] H. Kitahara, R. Ueji, N. Tsuji, Y. Minamino, *Acta Mater.* 54 (2006) 1279.
- [43] T.W. Heo, L.Q. Chen, *Acta Mater.* 76 (2014) 68.
- [44] Y.Z. Ji, A. Issa, T.W. Heo, J.E. Saal, C. Wolverton, L.Q. Chen, *Acta Mater.* 76 (2014) 259.
- [45] S. Bhattacharyya, T.W. Heo, K. Chang, L.-Q. Chen, *Modell. Simul. Mater. Sci. Eng.* 19 (2011) 035002.
- [46] S. Bhattacharyya, T.W. Heo, K. Chang, L.-Q. Chen, *Commun. Comput. Phys.* 11 (2012) 726.
- [47] J.W. Cahn, J.E. Hilliard, *J. Chem. Phys.* 28 (1958) 258–267.
- [48] J.W. Cahn, *J. Chem. Phys.* 30 (1959) 1121–1124.
- [49] J.W. Cahn, J.E. Hilliard, *J. Chem. Phys.* 31 (1959) 688–699.
- [50] H.M. Ledbetter, R.P. Reed, *J. Phys. Chem. Ref. Data* 2 (1973) 531–617.
- [51] H.W. Luo, J. Shi, C. Wang, W.Q. Chao, X.J. Sun, H. Dong, *Acta Mater.* 59 (2011) 4002–4014.
- [52] L. Liu, Z.-G. Yang, C. Zhang, W.B. Liu, *Mater. Sci. Eng. A* 527 (2010) 7204–7209.
- [53] L. Liu, PhD Dissertation, The Tsinghua University, 2012.